

# Coalescence of Molecular Filaments

Nanda Kumar (✉ [nanda@astro.up.pt](mailto:nanda@astro.up.pt))

Institute of Astrophysics and Space Science, Porto

Doris Arzoumanian

Centro de Astrofísica da Universidade do Porto

Alexander Men'shchikov

AIM, CEA, CNRS, Université Paris-Saclay, Université Paris Diderot

Pedro Palmeirim

Centro de Astrofísica da Universidade do Porto

Shu-Ichiro Inutsuka

Nagoya University

---

## Physical Sciences - Article

**Keywords:** Line Mass Spectrum, Star Formation, Surface Density Map, Multi-scale Decomposition, Isothermal Sphere Radial Profile

**Posted Date:** December 4th, 2020

**DOI:** <https://doi.org/10.21203/rs.3.rs-117331/v1>

**License:**  This work is licensed under a Creative Commons Attribution 4.0 International License.

[Read Full License](#)

---

# Coalescence of Molecular Filaments

Nanda Kumar<sup>1,\*</sup>, Doris Arzoumanian<sup>1</sup>, Alexander Men'shchikov<sup>2</sup>, Pedro Palmeirim<sup>1</sup>, and Shu-Ichiro Inutsuka<sup>3</sup>

<sup>1</sup>Centro de Astrofísica da Universidade do Porto, Rua das Estrelas, s/n, 4150-762, Porto, Portugal

<sup>2</sup>AIM, CEA, CNRS, Université Paris-Saclay, Université Paris Diderot, Sorbonne Paris Cité, F-91191 Gif-sur-Yvette, France

<sup>3</sup>Department of Physics, Nagoya University, Furo-cho, Chikusa-ku, Nagoya, Aichi 464-8602, Japan

\*corresponding author(s): Nanda Kumar (nanda@astro.up.pt)

## ABSTRACT

Star-forming molecular filaments are found to display a spectrum of line-masses (mass per unit length)<sup>1</sup>. This spectrum is thought to influence key observational parameters of star formation<sup>2</sup> including the core and stellar initial mass function<sup>1</sup>. The exact mechanism producing the wide-range of line-masses is unknown, even though, higher surface densities are often observed at the intersection of filaments in hub-filament systems<sup>3</sup>. Here we show that cascades of lower density filaments coalescing to form higher density filaments and eventually hubs. By performing a multi-scale decomposition of surface density maps of the MonR2 star-forming region, which displays a spiral-shaped hub-filament system<sup>4</sup>, the coalescence effect is detected in two consecutive cascading steps (the surface density jumps by an order of magnitude at each step) before merging at the central hub which is found to be a dense network of short high-density filaments (as opposed to its view as a massive clump). The radial density structure of the dense-gas component of the hub-filament system shows a power-law dependence of  $N_{H_2} \propto r^{-2}$  over the scale of  $\sim 5$  pc, a feature previously found only at scales of 0.1 pc in star-forming cores<sup>5</sup>. It appears that the hub-filament system is mimicking the radial profile of an isothermal sphere, at parsec scales, a feature not known until now. This behavior is not seen for the diffuse cloud ( $N_{H_2} \propto r^{-0.5}$ ) which holds nearly equal mass. The filamentary nature of the hub implies that only some (embedded in the filaments), and not all, stellar seeds within the hub can become massive stars.

## Main

Interstellar medium (ISM) is known to be filamentary both in its atomic<sup>6</sup> and molecular<sup>7</sup> forms. This view is firmly pronounced by data obtained with modern observational facilities with ever-increasing angular resolution and sensitivities<sup>8,9</sup>. A hierarchy of filamentary structures have been named to describe observational data; galactic spines<sup>10</sup>, giant filaments<sup>11</sup>, filaments<sup>9</sup>, fibers<sup>12</sup>, striations and strands<sup>8</sup>. This hierarchy is distinguished by the physical size, density and the total mass held within them. In the nearby ( $< 500$ pc) star-forming regions, filamentary structures span a range of  $\sim 3$  orders of magnitude in surface densities<sup>9</sup>. The resulting filament line-mass functions are thought to be the origin of dense core- and stellar- mass functions<sup>1</sup>. Massive star formation itself is shown to take place only at junctions of filaments called hubs<sup>3</sup>, that are found to be fed by longitudinal flows along filaments<sup>13</sup>. To assess the filament mass reservoir with respect to the hub, and examine if filamentary flows can substantially enhance the hub mass, we conducted a multi-scale multi-component analysis (see Methods) of the surface density maps of the Mon R2 star-forming region.

Among the nearby ( $< 1$  kpc) star-forming regions, Mon R2 ( $d = 830$  pc) is a unique hub-filament system with a miniature spiral galaxy appearance<sup>4</sup>, where the dense central hub is forming a cluster of stars including the B-type star Mon R2 (Fig.1). This large network of filaments is shown to be constrained in a flattened sheet-like space, based on an analysis of the velocity information from the observations of molecular emission lines<sup>4</sup>. The sheet has a low inclination angle of  $\sim 30^\circ$  with the plane of the sky giving its spiral galaxy appearance. Observations of Mon R2 region in five infrared bands, obtained with the *Herschel* space telescope was used to produce a surface (column) density map at high-angular resolution ( $11.4''$ )<sup>14</sup>. The structural components of the map were separated using algorithms to find filaments<sup>15</sup>, sources<sup>16</sup> and the extended non-filamentary emission (hereafter diffuse cloud)<sup>17</sup>. This allowed us to analyse the mutually uncontaminated surface density structure and mass of the individual filaments (Fig.1). Previous studies have only estimated the diffuse cloud based on measurements in regions void of filaments<sup>4</sup>, but here it is extracted by decomposition of the observed data.

The detected filaments appear in a range of lengths and surface densities all of which are radially converging to the central hub, where the density reaches its peak values. The cascades of lower density filaments are found to funnel into higher density filaments, which in turn coalesce to form even higher density filaments. Three such cascading groups are marked in Fig.2a with white boundaries, two of which funnel into the next step as marked by yellow boundary. At each step, the surface density is found to increase by a factor of  $\sim 5$ -10 and the length decreases. The coalescing steps display a net change in surface density

37 from  $\sim 5 \times 10^{20} \text{cm}^{-2}$  to  $\sim 2 \times 10^{23} \text{cm}^{-2}$ . Given that the filament networks are observed in projection, not all aligned features are  
38 actually coalescing. The containment of the filaments within the sheet-like geometry of the cloud enhances the probability  
39 of viewing several coalescing junctions, as evidenced by the measurable density jumps that are identified and marked in the  
40 figure. The jumps are prominent as the network gets denser moving to the radial converging point at the central hub ( $r = 0.8 \text{ pc}$ ).  
41 Analysis of the filaments angles shows that they are radially focused on to the hub centre toward Mon R2 source (see Fig. 2c, 2d  
42 and Methods). The mean deviation from the purely radial direction is an increasing function of the radial distance to the hub,  
43 suggesting that filament alignment is influenced by the gravitational potential of the hub. The radial alignment can enhance the  
44 incidence of filament coalescence. Coalescing filaments go through a junction resulting in higher line-density filament, but  
45 so are hubs, raising the question of which type of junctions lead to what? It appears that the angle of incidence of filaments  
46 forming the junction and the gravitational potential difference across the junction controls the final product. For example, acute  
47 angles are more likely to produce higher density filaments while obtuse angles may result in hubs. At a radial distance of 1 pc  
48 the number of filaments peak to a maximum (Fig. 2b), and at exactly the same position, the angles of the filaments deviate from  
49 the purely radial direction (Fig. 2c & 2d). This is an indication of the filaments bending, possibly due to the rotation of the hub  
50 with respect to the outer areas, especially so, because the density profile is smooth and shows no such breaks (Fig. 3).

51 The mass reservoir held within the filaments are marked in Fig. 1, and listed for all structural components in Table. 1. The  
52 central hub region within a radius of 0.8 pc holds  $\sim 1300 M_{\odot}$ , while  $\sim 800 M_{\odot}$  is held in the filaments located in the annular  
53 region of 0.8-2.5 pc. Therefore, a significant mass reservoir is available in the filaments if the currently B-type young star  
54 Mon R2 were to accrete further mass at rates of  $10^{-3}$ - $10^{-4} M_{\odot} \text{ yr}^{-1}$  as estimated from the observed longitudinal flows<sup>4</sup>. These  
55 accretion rates measured from lower spatial resolution observations concluded that the main filaments (higher density) transport  
56 mass to the central hub at a rate that is four times higher than the secondary filaments (lower density) to the main filaments. In  
57 the light of the coalescence mechanism discovered here, it appears that longitudinal flow rates may be simply proportional to  
58 the density of the host filament. In Table. 1 the mass held in filaments, diffuse cloud and compact sources are listed as a function  
59 of radial annuli. Comparing between the annuli, the relative mass held in the dense filaments are the highest in the hub and  
60 slowly declines away from the hub. The diffuse cloud displays a reverse trend (Table. 1). The number of compact sources also  
61 (naturally) follows the trend of the dense gas filaments. Compact sources on these column density maps trace both pre- and  
62 proto-stellar cores. If the core to star formation efficiency is taken as 50%, the listed source fraction in Table. 1 represents twice  
63 the star formation efficiency as a function of radius.

64 Given the extraordinary symmetry of the target, we studied the azimuthally averaged radial column density profile of the  
65 filaments- and diffuse-components in a  $5 \text{ pc} \times 5 \text{ pc}$  projected region centred on the Mon R2 hub (Fig. 3). The annular region  
66 excluding the hub ( $r = 0.8 \text{ pc}$ ) and extending up to 2 pc can be well fitted by power-law functions. The filaments and diffuse  
67 cloud components can be fitted respectively by power-law variations of surface density  $\Sigma \propto r^{-2}$  and  $\Sigma \propto r^{-0.5}$ , where  $r$  is the  
68 radius from the hub centre. The combined (filament+diffuse cloud, without the compact sources) component follow  $\Sigma \propto r^{-1}$   
69 relation. The observed image is very close to this relationship because the sources contribute a small fraction to the total  
70 surface density (sources mass fraction of 9%-15%, see Table. 1). The volume density ( $\rho$ ) profiles of proto-stellar envelopes are  
71 typically represented by  $\rho \propto r^{-2}$ , and it is indicative of an isothermal sphere in equilibrium or at the verge of collapse<sup>5</sup>. In  
72 Mon R2, given that the filaments are constrained in a sheet-like space, that is nearly in the plane of the sky, the observed  $\Sigma$   
73 profile is, in reality, representing the  $\rho$  profile. Therefore it appears that the hub-filament system is mimicking the radial profile  
74 of an isothermal sphere, at parsec scales, a feature not known until now. The hub itself is found to be a complex network of  
75 intertwined, very dense, short filaments and coincide with the dense cluster of young stars in the embedded cluster. This view  
76 of the hub as a close network of dense filaments stands in contrast to currently pervading ideas that hubs are similar to massive  
77 clumps<sup>3</sup>. Even though matter can be transported and fed to the stars inside the hub through longitudinal flows, in the new view,  
78 whether a star will benefit from it and gain mass depends on whether the star is embedded inside one of the dense filaments  
79 within the hub network. Therefore, only some, and not all, of the stellar seeds within the hub can become massive stars.

80 In its simplest form, the volume density of cold dense matter controls the process of star formation, consequently influencing  
81 the key observational parameters, as often demonstrated by the studies of probability density functions<sup>2</sup> such as rho-PDF  
82 (volume) and N-PDF (surface). This density function of clouds is considered to be the underlying feature that eventually  
83 propagates to produce the star-forming core-mass functions and consequently the stellar initial-mass-function<sup>1</sup>. The discovery  
84 of coalescence here suggest that the density spectrum is likely assembled over several dynamical scales in the life-time of  
85 molecular clouds. During this time, the density functions can also be influenced by the gravitational potential of clumps and  
86 hubs from within, and by external shock waves that could re-structure the cloud material, for example into sheets, enhancing  
87 the efficiency of coalescence as in the case of Mon R2 studied here.

## 88 Methods

89 **Surface density maps** The *Herschel* space telescope was used to image the Mon R2 region in five far-infrared bands at  $70 \mu\text{m}$ ,  
90  $160 \mu\text{m}$ ,  $250 \mu\text{m}$ ,  $350 \mu\text{m}$  and  $500 \mu\text{m}$ , through the HOBYS program<sup>18</sup>. These images were used to compute surface density at

91 the standard resolution of  $36''$  and a higher angular resolution of  $18.2''$ <sup>14</sup> corresponding to the resolution of the  $250\mu\text{m}$  image.  
92 Using the same method, a  $11.4''$  resolution map (corresponding to the beam at  $160\mu\text{m}$  band) was produced. Because the  
93  $160\mu\text{m}$  image may not be tracing the cold matter, we tested the fidelity of surface density map at  $11.4''$  resolution, by Gaussian  
94 smoothing to  $18.2''$  and  $36''$  and comparing with the  $18.2''$  high-res and  $36''$  standard resolution maps. While the total surface  
95 density remained conserved, the maps at different angular resolutions were locally comparable with an accuracy of 10%-20%.  
96 Such variations are expected due to redistribution of fluxes as a function of the resolution.

97  
98 **Filament, Diffuse cloud and source detection** The filaments, compact sources and the large scale diffuse background are  
99 decomposed on the surface density maps using the algorithm, *getsf* (Men'shchikov, 2021, submitted to AA). This is an updated  
100 and combined version of the widely used and tested algorithms namely: *getsources*<sup>16</sup>, *getfilaments*<sup>15</sup>, and *getimages*<sup>17</sup>. The  
101 method was developed for extracting dense cores and young stellar objects in far-infrared to sub-millimetre observations with  
102 the Herschel space telescope, even though it can be applied on any data set. There are many similarities between *getsf* and its  
103 predecessors, the most important new feature being the careful separation of the structural components based on their shapes.  
104 In the new method, the spatial decomposition of the observed image is conducted in a range of angular scales to identify the  
105 structural components and separate them. This allows disentangling features over multiple angular scales and separates the  
106 sources from filaments and backgrounds. The main processing steps of *getsf* are the spatial decomposition of the observed  
107 images, separation of the structural components, flattening of the detection images of the source and filament components, the  
108 combination of the detection images from different wavebands, detection of sources and filaments, and their measurements.  
109 The source detection algorithm is unchanged with respect to *getsources* and measurements of sources and filaments have been  
110 substantially improved. Here we have applied these methods on the surface density maps of Mon R2 at  $11.4''$  resolution.

111  
112 **Analysis of the filament components** The output from the *getsf* decomposition includes component images namely, filaments,  
113 diffuse cloud background, compact source, the sum of which correspond to the original surface density map. The filaments-  
114 image is a combination of filaments detected at multiple angular scales starting from  $16''$  to  $258''$ , a value defined by the user  
115 after an initial examination of the features in the input image. The skeletons, tracing the crest of the filament at each angular  
116 scale is produced by *getsf*. Additionally, the filaments lengths, widths, surface and linear densities are also produced. We  
117 combined the skeletons detected at all angular scales to produce a mask. This mask traces the crests of all detected filaments of  
118 varying lengths and widths. The filament component image was masked with the skeleton mask, to examine the crest column  
119 densities and its variation in the entire image, as shown in Fig.2.

120  
121 **Filament lengths and angles** For every skeleton, the average of the radial distances of all skeleton pixels was computed. This  
122 radial distance is plotted against the projected length of the skeleton in Fig. 2b. There appears to be a marginal indication  
123 that longer filaments are located farther away from Mon R2. In other words, as the filaments coalesce from lower to higher  
124 line-density objects, their length diminishes. Next, the number of filaments as a function of this average radial distance of  
125 skeleton pixels is plotted as a histogram in the same figure (Fig. 2b). It appears that the number of filament skeletons peak just  
126 at the boundary of the hub. To assess how the filaments are oriented around Mon R2 we computed the following. a) Divided  
127 the region around Mon R2 radially into many annuli with widths of  $dr=0.2$  pc. b) In each annulus, the average deviation  $\bar{\theta}$  of  
128 the filament angles from the purely radial direction was calculated. Next, an average  $\overline{\Delta\theta}$  was computed where  $\Delta\theta = \theta - \bar{\theta}$ .  
129 Plotting  $\bar{\theta}$  and  $\overline{\Delta\theta^2}$  as a function of the radius of the annulus, we note that the  $\bar{\theta}$  remains close to zero up to 3 pc suggesting  
130 that the filaments are oriented radially toward Mon R2. The  $\overline{\Delta\theta}$  is a slowly increasing function of radius beyond the "hub"  
131 suggesting that the filaments radial alignment is influenced by the gravitational field of the Mon R2 hub. The linear-fit for the  
132 region between 1 pc to 3.8 pc, is described by  $\Delta\theta^2 = 158 \times \text{Dist}(\text{pc}) + 943$ , with a correlation coefficient of 0.56.

133  
134 **Radial plots** Radial plots of surface density distribution were produced for the observed image, components of the filament  
135 and the diffuse background. Centered on the coordinates of Mon R2 at 06:07:45.6 -6:23:00, moving radially outward, one pixel  
136 width azimuthal average was computed up to a projected radial distance of 2.5 pc. The standard-deviation of the non-zero pixels  
137 in the azimuthal average is used as the error at each radial point. This allows us to produce a smoother curve that was fitted  
138 with power laws for the region with a radius between 0.8 pc and 2 pc. As evident in the plot shown in Fig. 3, the region interior  
139 to 0.8 pc, defined as the hub, shows an abrupt jump in the surface densities, whereas the region beyond the hub varies smoothly.

## 141 References

- 142 1. André, P., Arzoumanian, D., Könyves, V., Shimajiri, Y. & Palmeirim, P. The role of molecular filaments in the origin  
143 of the prestellar core mass function and stellar initial mass function. **629**, L4, [10.1051/0004-6361/201935915](https://doi.org/10.1051/0004-6361/201935915) (2019).  
144 [1907.13448](https://doi.org/10.1051/0004-6361/201935915).

- 145 2. Kainulainen, J., Federrath, C. & Henning, T. Unfolding the Laws of Star Formation: The Density Distribution of Molecular  
146 Clouds. *Science* **344**, 183–185, [10.1126/science.1248724](https://doi.org/10.1126/science.1248724) (2014). [1404.2722](https://arxiv.org/abs/1404.2722).
- 147 3. Kumar, M. S. N., Palmeirim, P., Arzoumanian, D. & Inutsuka, S. I. Unifying low- and high-mass star formation through  
148 density-amplified hubs of filaments. The highest mass stars (>100 M) form only in hubs. **642**, A87, [10.1051/0004-6361/  
149 202038232](https://doi.org/10.1051/0004-6361/202038232) (2020). [2008.00295](https://arxiv.org/abs/2008.00295).
- 150 4. Treviño-Morales, S. P. *et al.* Dynamics of cluster-forming hub-filament systems. The case of the high-mass star-forming  
151 complex Monoceros R2. **629**, A81, [10.1051/0004-6361/201935260](https://doi.org/10.1051/0004-6361/201935260) (2019). [1907.03524](https://arxiv.org/abs/1907.03524).
- 152 5. Ward-Thompson, D., Scott, P. F., Hills, R. E. & Andre, P. A Submillimetre Continuum Survey of Pre Protostellar Cores.  
153 **268**, 276, [10.1093/mnras/268.1.276](https://doi.org/10.1093/mnras/268.1.276) (1994).
- 154 6. Heiles, C. HI shells and supershells. **229**, 533–537, [10.1086/156986](https://doi.org/10.1086/156986) (1979).
- 155 7. Schneider, S. & Elmegreen, B. G. A catalog of dark globular filaments. **41**, 87–95, [10.1086/190609](https://doi.org/10.1086/190609) (1979).
- 156 8. André, P. *et al.* From Filamentary Networks to Dense Cores in Molecular Clouds: Toward a New Paradigm for Star  
157 Formation. In Beuther, H., Klessen, R. S., Dullemond, C. P. & Henning, T. (eds.) *Protostars and Planets VI*, 27,  
158 [10.2458/azu\\_uapress\\_9780816531240-ch002](https://doi.org/10.2458/azu_uapress_9780816531240-ch002) (2014). [1312.6232](https://arxiv.org/abs/1312.6232).
- 159 9. Arzoumanian, D. *et al.* Characterizing the properties of nearby molecular filaments observed with Herschel. **621**, A42,  
160 [10.1051/0004-6361/201832725](https://doi.org/10.1051/0004-6361/201832725) (2019). [1810.00721](https://arxiv.org/abs/1810.00721).
- 161 10. Goodman, A. A. *et al.* The Bones of the Milky Way. **797**, 53, [10.1088/0004-637X/797/1/53](https://doi.org/10.1088/0004-637X/797/1/53) (2014). [1408.0001](https://arxiv.org/abs/1408.0001).
- 162 11. Zucker, C., Battersby, C. & Goodman, A. Physical Properties of Large-scale Galactic Filaments. **864**, 153, [10.3847/  
163 1538-4357/aacc66](https://doi.org/10.3847/1538-4357/aacc66) (2018). [1712.09655](https://arxiv.org/abs/1712.09655).
- 164 12. Hacar, A., Tafalla, M. & Alves, J. Fibers in the NGC 1333 proto-cluster. **606**, A123, [10.1051/0004-6361/201630348](https://doi.org/10.1051/0004-6361/201630348)  
165 (2017). [1703.07029](https://arxiv.org/abs/1703.07029).
- 166 13. Peretto, N. *et al.* SDC13 infrared dark clouds: Longitudinally collapsing filaments? **561**, A83, [10.1051/0004-6361/  
167 201322172](https://doi.org/10.1051/0004-6361/201322172) (2014). [1311.0203](https://arxiv.org/abs/1311.0203).
- 168 14. Palmeirim, P. *et al.* Herschel view of the Taurus B211/3 filament and striations: evidence of filamentary growth? **550**,  
169 A38, [10.1051/0004-6361/201220500](https://doi.org/10.1051/0004-6361/201220500) (2013). [1211.6360](https://arxiv.org/abs/1211.6360).
- 170 15. Men'shchikov, A. A multi-scale filament extraction method: getfilaments. **560**, A63, [10.1051/0004-6361/201321885](https://doi.org/10.1051/0004-6361/201321885)  
171 (2013). [1309.2170](https://arxiv.org/abs/1309.2170).
- 172 16. Men'shchikov, A. *et al.* A multi-scale, multi-wavelength source extraction method: getsources. **542**, A81, [10.1051/  
173 0004-6361/201218797](https://doi.org/10.1051/0004-6361/201218797) (2012). [1204.4508](https://arxiv.org/abs/1204.4508).
- 174 17. Men'shchikov, A. Background derivation and image flattening: getimages. **607**, A64, [10.1051/0004-6361/201730925](https://doi.org/10.1051/0004-6361/201730925)  
175 (2017). [1707.09574](https://arxiv.org/abs/1707.09574).
- 176 18. Motte, F. *et al.* Initial highlights of the HOBYS key program, the Herschel imaging survey of OB young stellar objects.  
177 **518**, L77, [10.1051/0004-6361/201014690](https://doi.org/10.1051/0004-6361/201014690) (2010).

## 178 Acknowledgements

179 MSNK acknowledges the support from FCT - Fundação para a Ciência e a Tecnologia through Investigador contracts and  
180 exploratory project (IF/00956/2015/CP1273/CT0002). DA and PP acknowledge support from FCT/MCTES through Portuguese  
181 national funds (PIDDAC) by grant UID/FIS/04434/2019. PP receives support from fellowship SFRH/BPD/110176/2015 funded  
182 by FCT(Portugal) and POPH/FSE(EC).

## 183 Author contributions statement

184 MSNK envisioned the project, conducted general data analysis and wrote the paper, AM produced the high-res surface density  
185 images and decomposed them using the GETSF code, PP conducted the angle and length analysis, DA played a key role along  
186 with MSNK in developing main ideas and progressing the project, and SI proposed the angle analysis and pointed out the  
187 different behavior of dense and diffuse gas. All authors equally contributed through discussions.

## 188 Competing interests

189 There are no competing interests.

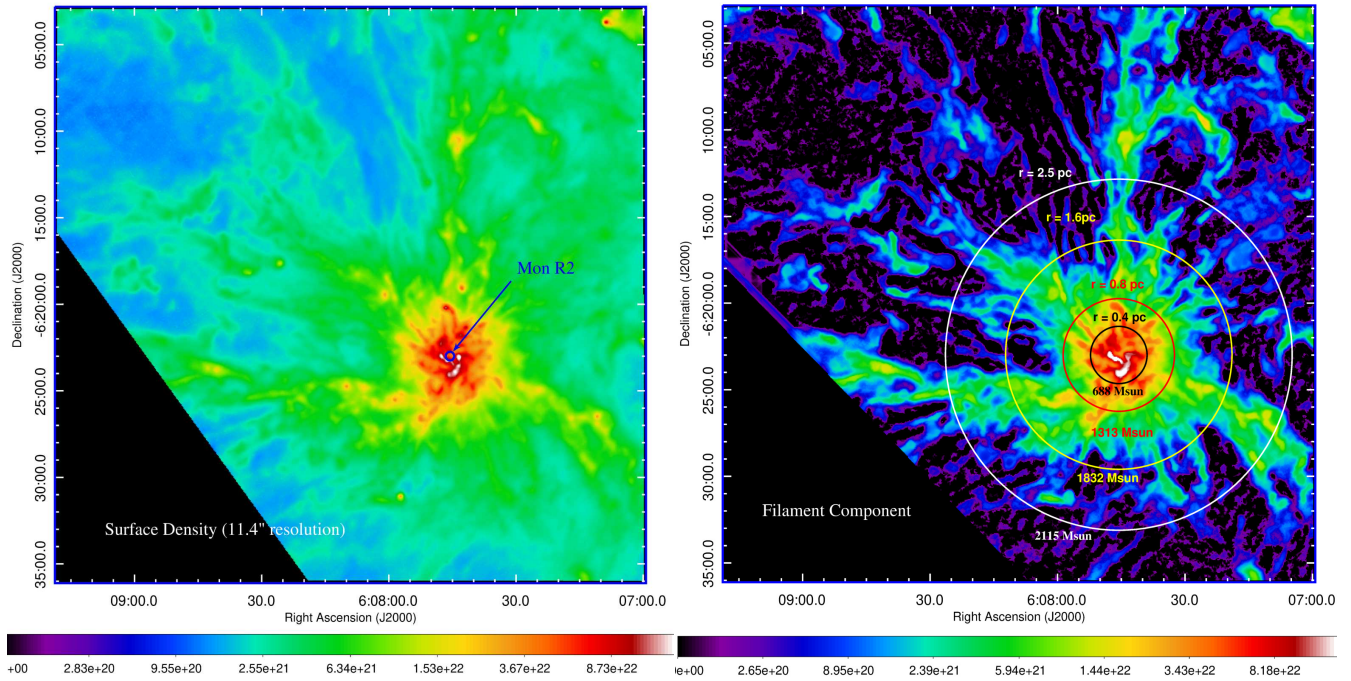


**Figure 1. Separating the Filaments:** Surface density map of the Mon R2 star forming region (left) and the decomposed "filaments-only" component (right). The horizontal color bar are in units of  $\text{cm}^{-2}$ . In the right panel, the total mass of the filaments enclosed within concentric circles of different radii are annotated in different colors. At a distance of 830 pc, the  $11.4''$  resolution correspond to a beam of 0.046 pc.

Radius (pc)	0.4 (core-hub)	0.8 (hub)	1.6	2.5
Filament Mass ( $M_{\odot}$ )	688	1313	1832	2115
Diffuse Cloud Mass ( $M_{\odot}$ )	89	251	732	1434
Compact Sources ( $M_{\odot}$ )	135	229	314	372
Total (Fil+DifCl+sources) Mass ( $M_{\odot}$ )	912	1794	2879	3921
Filament mass (%)	75	73	64	54
DiffCl mass (%)	10	14	25	37
Source mass(%)	15	13	11	9

**Table 1.** The mass inside filaments, diffuse cloud and compact sources as a function of radius. The percentage fraction of "source mass" represents twice star formation efficiency, assuming a core to star efficiency of 50%.

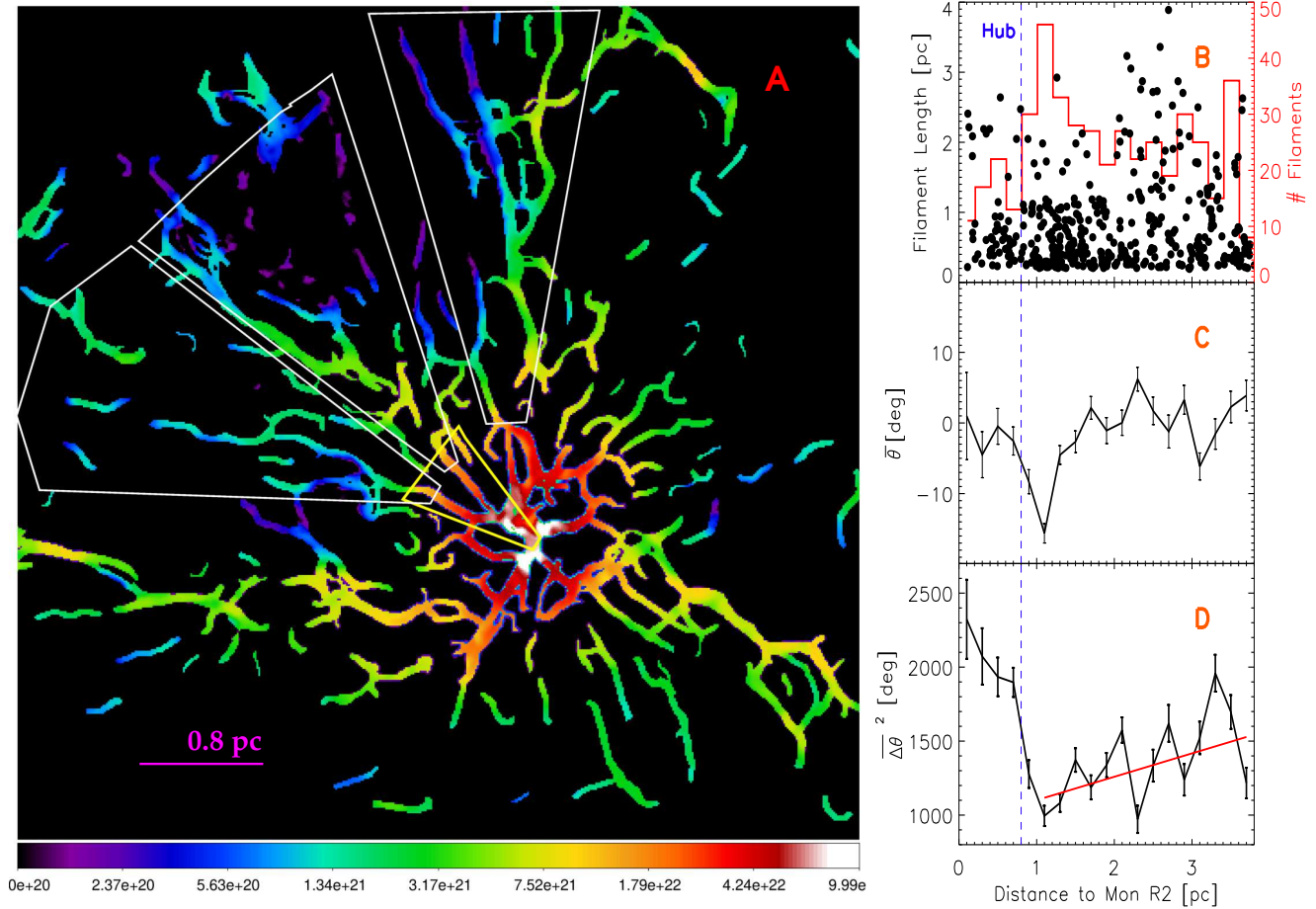


**Figure 2. Skeleton analysis:** a) Average of filament skeletons detected over multiple angular scales from  $16''$  up to  $258''$  are used as a mask on the filament-component image. Groups of coalescing filaments are enclosed by white line boundaries. Notice the density jumps at each level of coalescence. For example, two groups marked in white funnels into the filaments marked by the yellow boundary, finally merging in the hub region to form the network of the densest portions seen in white, representing a density of  $2 \times 10^{23} \text{ cm}^{-2}$ . b) Longer filaments are farther away from the hub, and the number of filaments appear to peak at the hub boundary, corresponding to the change in angles (see c & d), c) average filament angle with respect to the purely radial direction as a function of distance to Mon R2, show that they are radially aligned, d) deviation of the filament angle from the purely radial direction to Mon R2 is an increasing function of distance to Mon R2 suggesting an influence of the hub gravitational potential in aligning the filaments.

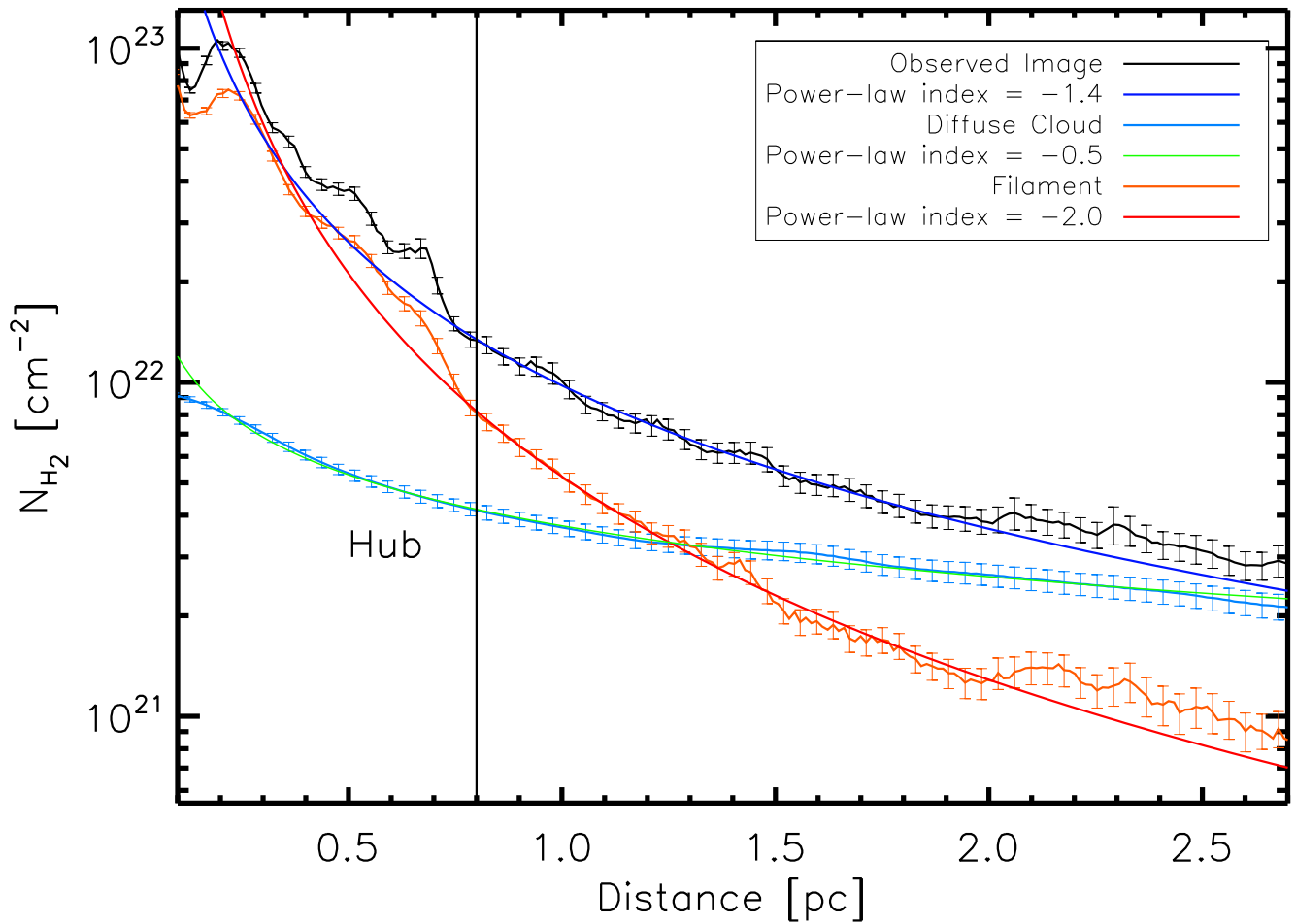


**Figure 3.** The radial profiles of azimuthal average of surface density centred on the MonR2 hub, as distributed in its structural components. The observed image radial profile is compared with separated filaments and diffuse cloud. The fitted curves and their power-law indices are listed for each component. The fit is performed for regions beyond 1 pc, excluding the hub. Error bars represent standard deviation of the non-zero values in each pixel annulus.

# Figures

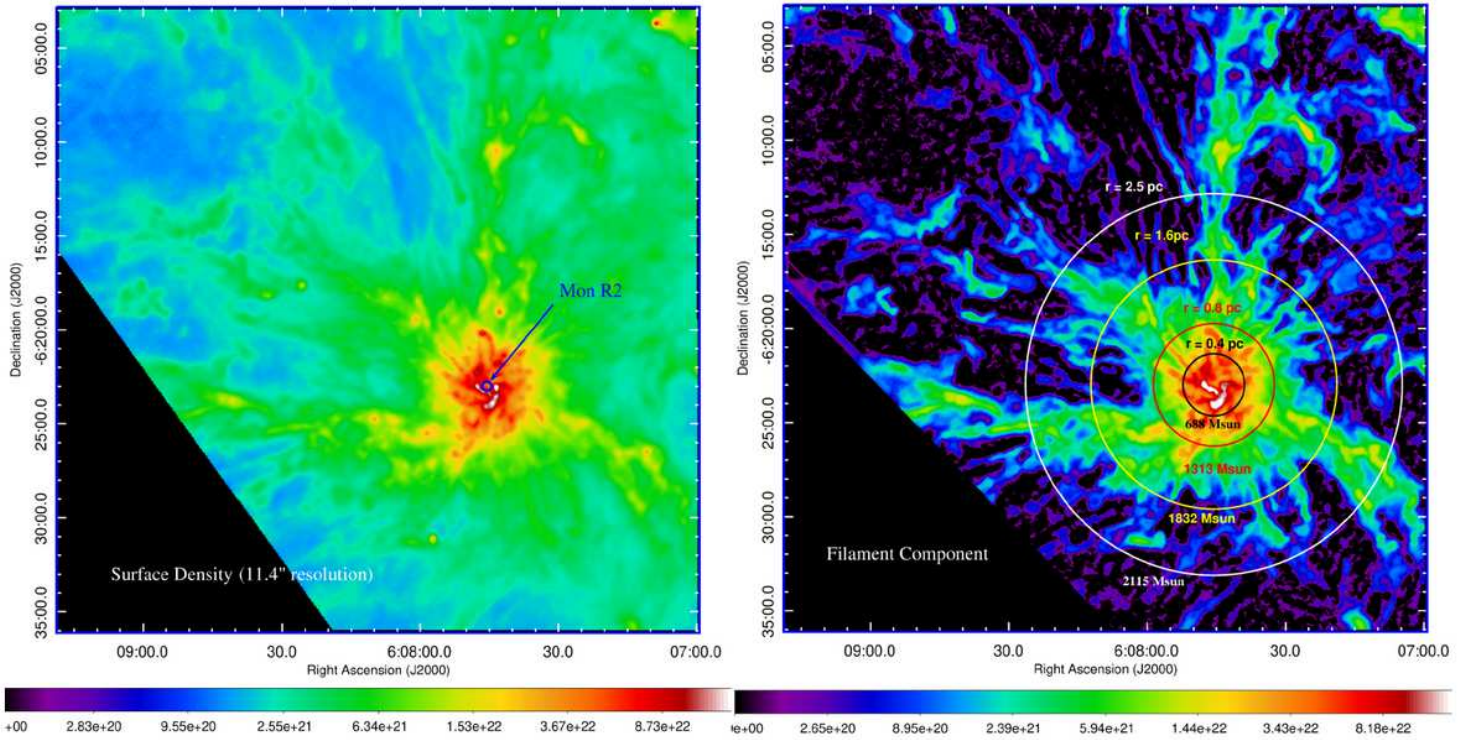
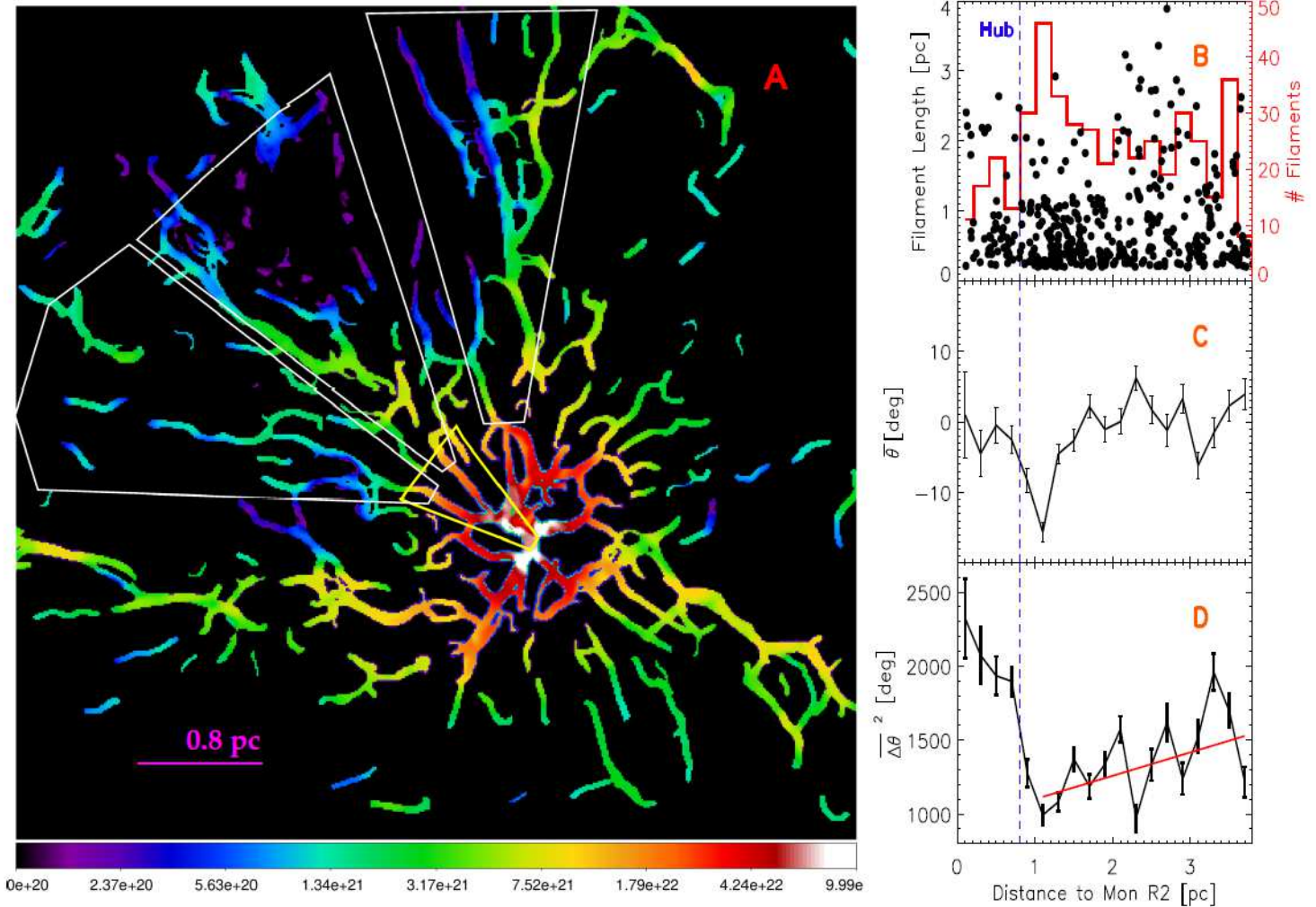


Figure 1

Separating the Filaments: Surface density map of the Mon R2 star forming region (left) and the decomposed "filaments-only" component (right). The horizontal color bar are in units of cm<sup>-2</sup>. In the right panel, the total mass of the filaments enclosed within concentric circles of different radii are annotated in different colors. At a distance of 830 pc, the 11.4'' resolution correspond to a beam of 0.046 pc.



**Figure 2**

Skeleton analysis: a) Average of filament skeletons detected over multiple angular scales from 16" up to 258" are used as a mask on the filament-component image. Groups of coalescing filaments are enclosed by white line boundaries. Notice the density jumps at each level of coalescence. For example, two groups marked in white funnels into the filaments marked by the yellow boundary, finally merging in the hub region to form the network of the densest portions seen in white, representing a density of  $2 \times 10^{23} \text{cm}^{-2}$ . b) Longer filaments are farther away from the hub, and the number of filaments appear to peak at the hub boundary, corresponding to the change in angles (see c & d), c) average filament angle with respect to the purely radial direction as a function of distance to Mon R2, show that they are radially aligned, d) deviation of the filament angle from the purely radial direction to Mon R2 is an increasing function of distance to Mon R2 suggesting an influence of the hub gravitational potential in aligning the filaments.

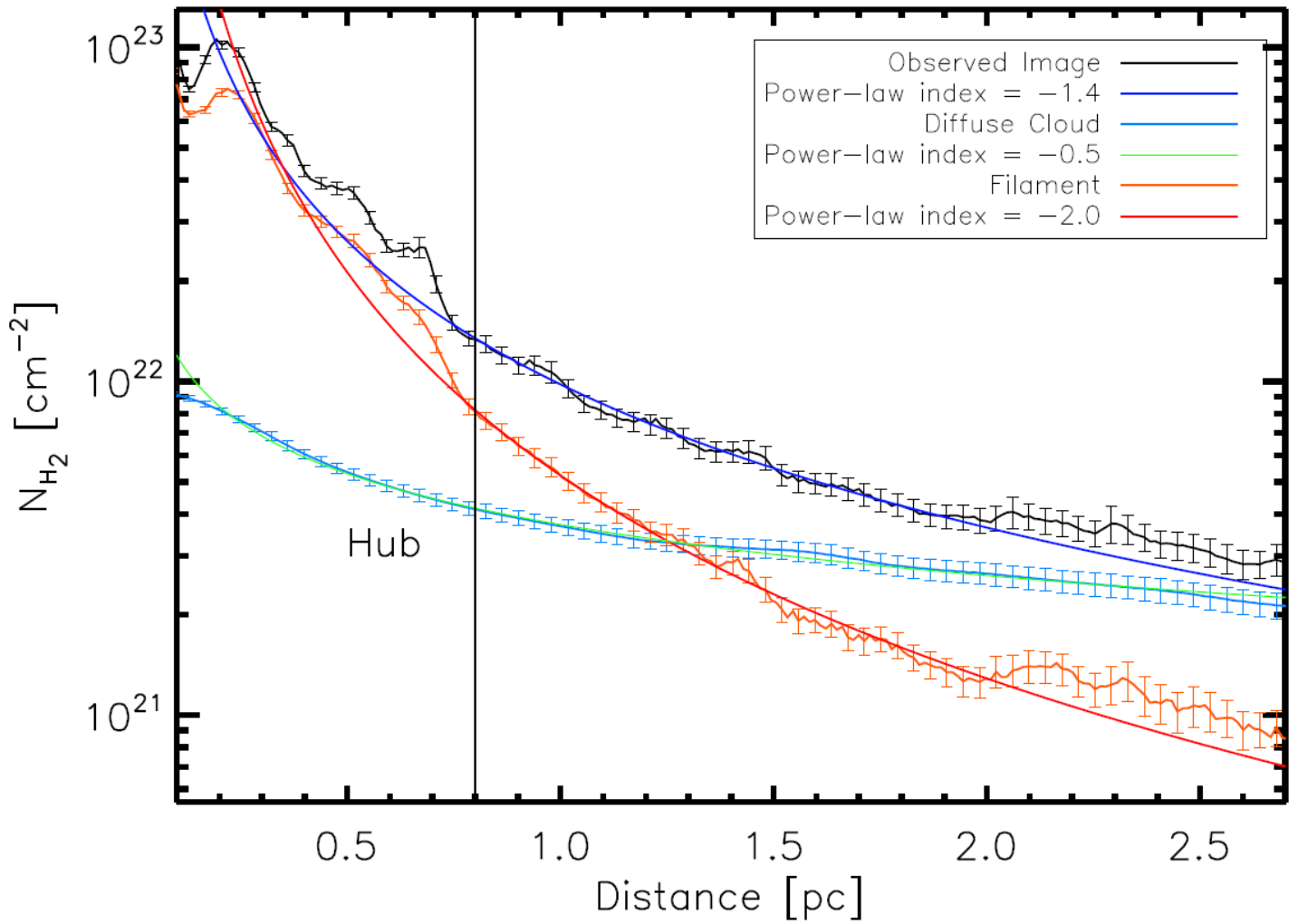


**Figure 3**

The radial profiles of azimuthal average of surface density centred on the MonR2 hub, as distributed in its structural components. The observed image radial profile is compared with separated filaments and diffuse cloud. The fitted curves and their power-law indices are listed for each component. The fit is performed for regions beyond 1 pc, excluding the hub. Error bars represent standard deviation of the non-zero values in each pixel annulus.